ATLAS NOTE

ATLAS-CONF-2012-145

November 9, 2012

Search for gluino pair production in final states with missing transverse momentum and at least three b-jets using 12.8 fb^{-1} of pp collisions at $\sqrt{s}$ = 8 TeV with the ATLAS Detector.

The ATLAS Collaboration

ATLAS-CONF-2012-145
12 November 2012

Abstract

The results of a search for gluino pair production with multi-b-jets final states in 12.8 fb^{-1} of pp collisions at $\sqrt{s} = 8$ TeV using the ATLAS detector at the LHC are reported. This search is performed in events with large missing transverse momentum, greater than or equal to four or six jets and at least three jets originating from b-quarks. No excess has been found in data with respect to the Standard Model predictions. Results are interpreted in the context of simplified models consisting of a gluino octet and a lightest supersymmetric particle $\tilde{\chi}_1^0$, with gluinos decaying in top or bottom quarks. In case of $\tilde{g} \to t\bar{t}\tilde{\chi}_1^0$ ($\tilde{g} \to b\bar{b}\tilde{\chi}_1^0$), gluino masses below 1150 (1240) GeV are excluded for LSP masses below 200 GeV.

1 Introduction

Supersymmetry (SUSY) [1–9] provides an extension of the Standard Model (SM) which resolves the hierarchy problem [10–13] by introducing supersymmetric partners for Standard Model particles. In the framework of the *R*-parity conserving minimal supersymmetric extension of the SM (MSSM) [14–18], SUSY particles are produced in pairs and the lightest supersymmetric particle (LSP) is stable, providing a possible candidate for dark matter. In a large variety of models, the LSP is the lightest neutralino ($\tilde{\chi}_1^0$). The coloured superpartners of quarks and gluons, the squarks ($\tilde{q}$) and gluinos ($\tilde{g}$), if not too heavy, would be produced in strong interaction processes at the Large Hadron Collider (LHC) and decay via cascades ending with the LSP. The undetected LSP results in missing transverse momentum – whose magnitude is referred to as $E_{\mathrm{T}}^{\mathrm{miss}}$ – while the rest of the cascade yields final states with multiple jets and possibly leptons. In the MSSM, the SUSY partners of the right-handed and left-handed quarks, $\tilde{q}_R$ and $\tilde{q}_L$, can mix to form two mass eigenstates $\tilde{q}_1$ and $\tilde{q}_2$. The mixing effect is proportional to the masses of the SM fermion partners and can therefore be large for the third generation. This may lead to the lightest sbottom ($\tilde{b}_1$) and stop ($\tilde{t}_1$) mass eigenstates being much lighter than the other squarks. As a consequence, $\tilde{b}_1$ and $\tilde{t}_1$ could be produced with relatively large cross-sections at the LHC, either directly in pairs, or through $\tilde{g}\tilde{g}$ production followed by $\tilde{g} \to \tilde{b}_1 b$ or $\tilde{g} \to \tilde{t}_1 t$ decays.

This note extends the search for gluino pair production in final states with at least 3 *b*-jets at ATLAS [19], which used 4.7 fb^{-1} of data collected in 2011 at a centre-of-mass energy of 7 TeV. The present analysis comprises a dataset of 12.8 fb^{-1} collected during the first half of 2012 at a centre-of-mass energy of 8 TeV and is based on a similar selection that requires large $E_{\mathrm{T}}^{\mathrm{miss}}$, no electron or muon and at least three jets identified as originating from *b*-quarks (*b*-jets) in the final state. Results are interpreted in two simplified models, hereafter denoted *G*tt and *G*bb, where the gluinos are assumed to decay through off-shell stops or sbottoms to $t\bar{t}\tilde{\chi}_1^0$ or $b\bar{b}\tilde{\chi}_1^0$, respectively.

2 The ATLAS detector

The ATLAS detector [20] consists of inner tracking devices surrounded by a superconducting solenoid, electromagnetic and hadronic calorimeters and a muon spectrometer with three large superconducting air-core toroid magnets. The inner detector, in combination with the 2 T field from the solenoid, provides precision tracking of charged particles for $|\eta| < 2.5$[1]. It consists of a silicon pixel detector, a silicon strip detector and a straw tube tracker that also provides transition radiation measurements for electron identification. The calorimeter system covers the pseudorapidity range $|\eta| < 4.9$. It is composed of sampling calorimeters with either liquid argon (LAr) or scintillating tiles as the active medium. The muon spectrometer has separate trigger and high-precision tracking chambers which provide muon identification and momentum measurement for $|\eta| < 2.7$.

[1] ATLAS uses a right-handed coordinate system with its origin at the nominal interaction point (IP) in the centre of the detector and the *z*-axis along the beam pipe. The *x*-axis points from the IP to the centre of the LHC ring, and the *y* axis points upward. Cylindrical coordinates (r, ϕ) are used in the transverse plane, ϕ being the azimuthal angle around the beam pipe. The pseudorapidity is defined in terms of the polar angle θ as $\eta = -\ln\tan(\theta/2)$.The distance ΔR in the $\eta - \phi$ space is defined as $\Delta R = \sqrt{(\Delta\eta)^2 + (\Delta\phi)^2}$.

3 Monte Carlo simulation

Samples of simulated events are used to model the background and the SUSY signals. The dominant sources of background come from processes with b-quarks in the final state. Monte Carlo (MC) samples of $t\bar{t}$ events are generated using POWHEG [21] interfaced to PYTHIA6 [22] and the Next-to-Leading Order (NLO) parton distribution function (PDF) set CT10 [23]. The distinction between the reducible background $t\bar{t}$ + jets and the irreducible backgrounds $t\bar{t}$ + b and $t\bar{t}$ + $b\bar{b}$, which are estimated separately, is performed at the truth level. Single top production is generated using AcerMC [24] interfaced to PYTHIA6 [22] and the PDF set CTEQ6L1 [25] for the t-channel, and using MC@NLO [26] interfaced to HERWIG [27] and JIMMY [28] with the PDF set CT10 [23] for the s-channel and Wt processes. The W and Z events produced in association with light- and heavy-flavour jets are generated with SHERPA [29] with up to 4 additional partons in the matrix element, treating b-quarks as massive in the calculation, and using the PDF set CT10 [23]. Diboson events are generated with up to three additional partons in the matrix element using SHERPA [29] and the PDF set CT10 [23]. Samples of $t\bar{t}$+W and $t\bar{t}$+Z events are generated with MADGRAPH [30] interfaced to PYTHIA6 [22] and with the PDF set CTEQ6L1 [25]. The signal samples are generated using Herwig++ [30] and the PDF set CTEQ6L1 [25]. The MC samples are processed either through a full simulation [31] of the ATLAS detector based on GEANT4 [32] or a fast simulation based on the parameterisation of the performance of the ATLAS electromagnetic and hadronic calorimeters. The effect of multiple pp interactions per bunch crossing is taken into account in the simulation. For the comparison with data, all SM background cross-sections are normalised to the results of higher-order calculations.

4 Object reconstruction

Jets are reconstructed from three-dimensional calorimeter energy clusters using the anti-k_t jet algorithm [33, 34] with a distance parameter of 0.4. The measured jet energy is corrected for inhomogeneities and for the non-compensating nature of the calorimeter by weighting differently energy deposits arising from electromagnetic and hadronic showers using correction factors derived from Monte Carlo simulations and validated with data [35]. An additional calibration is subsequently applied to the corrected jet energies relating the response of the calorimeter to true jet energy. The impact of additional collisions in the same or neighbouring bunch crossings is also taken into account using offset corrections derived as a function of the average number of interactions per bunch crossing $< \mu >$ and of the number of primary vertices N_{PV}. Only jets with $|\eta| < 4.5$ and $p_{\mathrm{T}} > 20$ GeV after calibration are retained. Events are rejected if they include jets failing the quality criteria described in Ref. [35]. To further reject spurious jet signals, additional criteria are applied on the charged p_{T} fraction f_{ch}, defined as the fraction of the transverse momentum of the jet carried by charged tracks, and on the fraction of the jet energy contained in the electromagnetic layers of the calorimeter f_{em}. Events are rejected if either of the two leading jets with $p_{\mathrm{T}} > 100$ GeV and $|\eta| < 2.0$ satisfies $f_{\mathrm{ch}} < 0.02$ or $f_{\mathrm{ch}} < 0.05$ and $f_{\mathrm{em}} > 0.9$. Except during the $E_{\mathrm{T}}^{\mathrm{miss}}$ computation, only jets with $|\eta| < 2.8$ are further considered.

A neural-network-based algorithm [36] is used to identify jets containing a b-hadron decay. This uses as inputs the output weights of different algorithms exploiting the impact parameter of the inner detector tracks, the secondary vertex reconstruction and the topology of b- and c-hadron decays inside the jet. The algorithm used has an efficiency of 75% for tagging b-jets in a MC sample of $t\bar{t}$ events with a rejection factor of 58, 4 and 8 against light quarks, c-quarks and τ leptons respectively. The b-jets are identified within the nominal acceptance of the inner

detector ($|\eta| < 2.5$) and are required to have $p_{\mathrm{T}} > 20$ GeV. To compensate for the differences between the b-tagging efficiencies and the mistag rates in data and MC simulation, b-tagging scale factors are applied to each jet in the simulations, as described in Refs. [36–38].

Electrons are reconstructed from energy clusters in the electromagnetic calorimeter associated to tracks in the inner detector. Electron candidates are required to have $p_{\mathrm{T}} > 20$ GeV and $|\eta| < 2.47$ and must satisfy the shower shape and track selection criteria described in Ref. [39]. Muon candidates are identified using a match between an extrapolated inner detector track and one or more track segments in the muon spectrometer, and are required to have $p_{\mathrm{T}} > 10$ GeV and $|\eta| < 2.4$.

To resolve overlaps between reconstructed jets and leptons, jets within a distance of $\Delta R = 0.2$ of an electron candidate are rejected. Furthermore, any lepton candidate with a distance $\Delta R < 0.4$ to the closest remaining jet is discarded. Events containing any remaining electrons and muons are vetoed in the signal, control and validation regions defined in Tables 1, 2 and 3.

The measurement of the missing transverse momentum two-dimensional vector (and its magnitude $E_{\mathrm{T}}^{\mathrm{miss}}$) is based on the transverse momenta of all jets, electron and muon candidates and all calorimeter cells not associated to such objects.

5 Event selection

Events are selected using triggers based on $E_{\mathrm{T}}^{\mathrm{miss}}$. This trigger is fully efficient for this analysis, which requires at least one jet, which is not required to be tagged as a b-jet, with $p_{\mathrm{T}} > 90$ GeV and $E_{\mathrm{T}}^{\mathrm{miss}} > 150$ GeV at the offline reconstruction stage. Events must pass basic quality criteria to reject detector noise and non-collision backgrounds. They are also required to have a reconstructed primary vertex associated with five or more tracks with $p_{\mathrm{T}} > 0.4$ GeV; when more than one such vertex is found, the vertex with the largest summed p_{T}^2 of the associated tracks is chosen as the primary vertex. Events are required to have at least three b-tagged jets with $p_{\mathrm{T}} > 30$ GeV. Events are then divided into two overlapping classes based on the number of jets (N_J) with $|\eta| < 2.8$ and $p_{\mathrm{T}} > 50$ GeV. The first class has $N_J \geq 4$ and the additional requirement that at least three of the b-tagged jets have $p_{\mathrm{T}} > 50$ GeV. The second class has $N_J \geq 6$ with no additional requirements on the b-tagged jets.

Three variables are calculated from the reconstructed objects to further select the events: $\mathrm{m}_{\mathrm{eff}}^{\mathrm{incl}}$, $\mathrm{m}_{\mathrm{eff}}^{\mathrm{4j}}$ and $\Delta\phi_{\mathrm{min}}^{4j}$. The inclusive effective mass $\mathrm{m}_{\mathrm{eff}}^{\mathrm{incl}}$, defined as the scalar sum of the $E_{\mathrm{T}}^{\mathrm{miss}}$ and the p_{T} of all jets with $p_{\mathrm{T}} > 30$ GeV, is correlated with the overall mass scale of the hard-scattering and provides good discrimination against SM background. The exclusive effective mass $\mathrm{m}_{\mathrm{eff}}^{\mathrm{4j}}$ is defined as the scalar sum of the $E_{\mathrm{T}}^{\mathrm{miss}}$ and the p_{T} of the four leading jets. It is used to suppress the multi-jet background and to define the signal regions targeting gluino decay $\tilde{g} \to b\bar{b}\tilde{\chi}_1^0$ where only four jets are expected in the final state. The $\Delta\phi_{\mathrm{min}}^{4j}$ is defined as the minimum azimuthal separation between any of the four leading jets and the missing transverse momentum direction. Placing the requirements $\Delta\phi_{\mathrm{min}}^{4j} > 0.4$ and $E_{\mathrm{T}}^{\mathrm{miss}}/\mathrm{m}_{\mathrm{eff}}^{\mathrm{4j}} > 0.2$ reduces the amount of multi-jet background, where $E_{\mathrm{T}}^{\mathrm{miss}}$ results from mis-reconstructed jets or from neutrinos emitted close to the direction of the jet axis.

Two sets of signal regions are defined which yield good signal sensitivity for the two models considered here. They are characterised by having $E_{\mathrm{T}}^{\mathrm{miss}} > 200$ GeV, at least four (SR4) or six (SR6) jet candidates, at least three b-tagged jets with $p_{\mathrm{T}} > 50$ (SR4) or 30 (SR6) GeV, no electron or muon, and are further classified as loose (L), medium (M) or tight (T) depending on the effective mass thresholds. The requirements that characterise each signal region are summarised in Table 1.

Common criteria: lepton veto, $p_{\mathrm{T}}^{j_1} > 90$ GeV, $E_{\mathrm{T}}^{\mathrm{miss}} > 200$ GeV, ≥ 3 b-jets, $E_{\mathrm{T}}^{\mathrm{miss}}/\mathrm{m}_{\mathrm{eff}}^{4\mathrm{j}} > 0.2$, $\Delta\phi_{\mathrm{min}}^{4j} > 0.4$			
SR	N_J ($p_{\mathrm{T}} > 50$ GeV)	p_{T} b-jets	$\mathrm{m}_{\mathrm{eff}}$
SR4-L/M/T	≥ 4 jets	> 50 GeV	$\mathrm{m}_{\mathrm{eff}}^{4\mathrm{j}} > 900/1100/1300$ GeV
SR6-L/M/T	≥ 6 jets	> 30 GeV	$\mathrm{m}_{\mathrm{eff}}^{\mathrm{incl}} > 1100/1300/1500$ GeV

Table 1: Definition of the six signal regions based on the number of jets (N_J), the b-jets p_{T} and the effective mass.

6 Background estimate

The main source of reducible background is the production of $t\bar{t}$ events in association with additional jets (apart from $t\bar{t}$+$b/b\bar{b}$) followed by the leptonic decay of one W boson, where the lepton is not reconstructed, or is outside of acceptance, or is mis-identified as a jet, or is a tau which decays hadronically. This background is estimated by normalising the MC event yield in the signal region to the event yield observed in a $t\bar{t}$-dominated control region. Systematic uncertainties that are correlated between the control and the signal regions largely cancel out in this procedure. Additional sources of reducible background are single top, $t\bar{t}$+W/Z and W/Z+heavy-flavour jets. Their contributions are taken from MC simulations and account for 10 to 20% of the total background depending on the signal region. The irreducible background $t\bar{t}$+$b/b\bar{b}$ is also estimated from MC simulation and accounts for up to 25% of the total background in the signal regions. The reducible contribution from multi-jet events is estimated using a data-driven method, based on a jet response smearing technique [40], and is found to be negligible in all control and signal regions.

Two control regions where the $t\bar{t}$+jets background accounts for about 80% of the total yield are defined by applying the same jet requirements and lepton veto as in the signal regions, but requiring exactly two b-jets instead of three or more. The requirements on $E_{\mathrm{T}}^{\mathrm{miss}}$ and $\mathrm{m}_{\mathrm{eff}}$ are relaxed in the control regions to minimise the statistical uncertainty and reduce the contribution from possible SUSY signal events. The definition of the two control regions is summarised in Table 2. The distributions of the missing transverse momentum and the effective mass in the two control regions for both data and MC expectation, normalised to cross-section times integrated luminosity, are shown in Figure 1.

Common criteria: lepton veto, $p_{\mathrm{T}}^{j_1} > 90$ GeV, $E_{\mathrm{T}}^{\mathrm{miss}} > 150$ GeV, $= 2$ b-jets, $E_{\mathrm{T}}^{\mathrm{miss}}/\mathrm{m}_{\mathrm{eff}}^{4\mathrm{j}} > 0.2$, $\Delta\phi_{\mathrm{min}}^{4j} > 0.4$				
CR	N_J ($p_{\mathrm{T}} > 50$ GeV)	p_{T} b-jets	$\mathrm{m}_{\mathrm{eff}}$	corresponding SR
CR4	≥ 4 jets	> 50 GeV	$\mathrm{m}_{\mathrm{eff}}^{4\mathrm{j}} > 500$ GeV	SR4-L, SR4-M, SR4-T
CR6	≥ 6 jets	> 30 GeV	$\mathrm{m}_{\mathrm{eff}}^{\mathrm{incl}} > 600$ GeV	SR6-L, SR6-M, SR6-T

Table 2: Definition of the two control regions used to estimate the $t\bar{t}$ background.

The background predictions have been further validated using a data-driven method that simultaneously estimates all SM background contributions with at least one misidentified b-jet. This method consists of predicting the number of jets originating from b-quarks in each event by solving a system of equations based on the number of b-tagged and non b-tagged jets

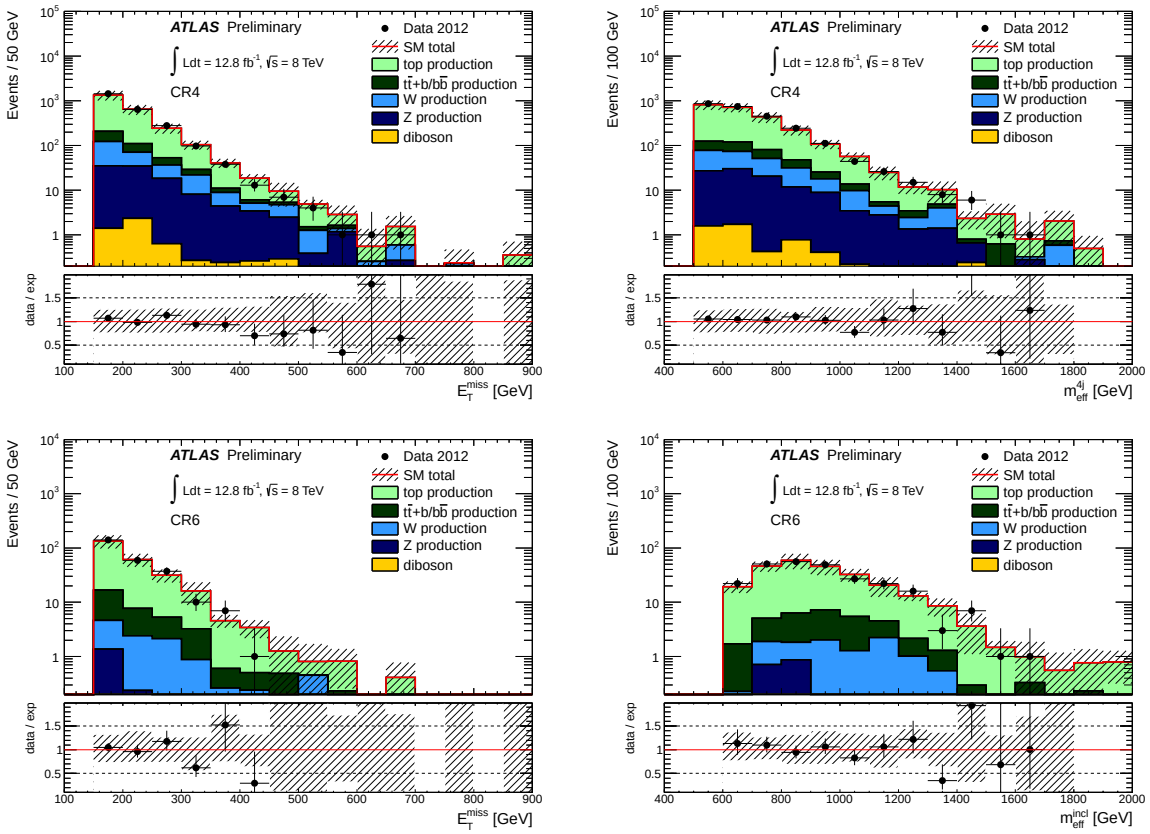

Figure 1: Distribution of the missing transverse momentum (left) and effective mass (right) in the CR4 (top) and CR6 (bottom) control regions. The effective mass definition corresponds to m_{eff}^{4j} and $m_{\mathrm{eff}}^{\mathrm{incl}}$ in CR4 and CR6, respectively. The MC expectation is normalised to cross-section times integrated luminosity. The hatched band shows the statistical uncertainty on the simulated event samples combined with the detector related systematic uncertainty (among which jet energy scale and b-tagging uncertainties are dominant). The histogram labelled "top production" includes the contribution from $t\bar{t}$ +jets, $t\bar{t}+W/Z$ and single top production. The bottom panel in each figure shows the ratio between the observed distribution and that predicted for the SM background.

in the event, along with the b-tagging efficiency and mistag rates. The b-tagging efficiency is measured in data using a combination of the ${p_{\mathrm{T}}}^{rel}$ and System8 methods described in Ref. [36]. The b-tagging mistag rate is determined in data and $t\bar{t}$ MC simulations using a control region enriched in top events. Consistent background predictions with respect to the baseline method have been found in all signal regions.

7 Systematic uncertainties

The dominant detector-related systematic effects are due to the jet energy scale (JES) and resolution (JER) uncertainties, and the uncertainty on the b-tagging efficiency and mistag rates. The JES uncertainty is derived from a combination of simulations, test beam data and in-situ measurements [35,41]. Additional contributions accounting for jet flavour composition, calorimeter response to different jet flavours, close-by jets, pileup and b-jet uncertainties are taken into account. Uncertainties on the JER are obtained with an in-situ measurement of the jet response asymmetry in di-jet events. These uncertainties on jets are propagated to the $E_{\mathrm{T}}^{\mathrm{miss}}$ measurement, and additional uncertainties on $E_{\mathrm{T}}^{\mathrm{miss}}$ arising from energy deposits not associated with any reconstructed objects are also included. The b-tagging uncertainty is evaluated by varying the η-, p_{T}- and flavour-dependent scale factors applied to each jet in the simulation within a range that reflects the systematic uncertainty on the measured tagging efficiency and mistag rates.

The systematic uncertainties in the modelling of the $t\bar{t}$+jets background are assessed as follows: the uncertainty due to the choice of the MC generator is estimated by comparing `POWHEG` to the leading-order `ALPGEN` generator [42] interfaced to `JIMMY` [28] and using the PDF set `CTEQ6L1` [25]; the parton shower (PS) uncertainty is assessed by comparing `POWHEG` [21] interfaced to `PYTHIA6` [22] to `POWHEG` [21] interfaced to `JIMMY` [28], both with the PDF set `CT10` [23]; the uncertainty due the initial (ISR) and final (FSR) state radiation is estimated by comparing `AcerMC` [24] MC samples, interfaced to `PYTHIA6` [22] and using the PDF set `CTEQ6L1` [25], generated with modified ISF/FSR modelling. The choice of the variation of the ISR/FSR parameters has been validated with data in an analysis of rapidity gaps between jets in $t\bar{t}$ events [43]. Uncertainties on the NLO W and Z cross-sections include renormalisation and factorisation scales, PDF and α_s uncertainties. An uncertainty of 60% is considered on the cross-section of the W production in association with b-quarks. Uncertainties of 100% are assumed for the cross-section of $t\bar{t}$ and Z events produced in association with b-quarks. For $t\bar{t}$+W/Z production, an uncertainty of 50% is assumed on the NLO cross-section. An additional uncertainty of 3.6% on the integrated luminosity, measured using techniques similar to that of Ref. [44], is included for all signal and background MC simulations.

8 Background fit

The $t\bar{t}$+jets yield in each signal region is extrapolated from the measured number of events in the corresponding control region (as per Table 2) using a fit based on the profile likelihood method [45]. Each control region is fitted separately, assuming no signal events. The only free parameter in each fit is the $t\bar{t}$+jets overall normalisation scale, while the shapes are taken from the MC simulation. The contributions from subdominant background processes are set at the expected values and allowed to vary within their respective uncertainties. The systematic uncertainties discussed in section 7 are treated as nuisance parameters constrained with a Gaussian function with a width corresponding to the size of the uncertainty considered, and

the correlations are taken into account where appropriate. The likelihood function is built as the product of Poisson probability density functions, describing the event counts in each region, and the constraints on the nuisance parameters.

To validate the reliability of the background fits, the results are extrapolated to validation regions kinematically located between the control and the signal regions.The data in the validation region is not itself used as a constraint by the fit, but is used to compare the results of the fit to statistically independent observations. Two validation regions are defined for each control region. They are defined with the same criteria as the signal regions, except for m_{eff} and E_T^{miss}. The definition of these validation regions is summarised in Table 3. The results of the background fit to the control regions extrapolated to the validation regions are shown in Tables 4 and 5. Nominal MC expectations (normalised to MC cross-sections) for the $t\bar{t}$+jets and the total backgrounds are given for comparison. The fitted values of the normalisation factors for $t\bar{t}$+jets are compatible with one and the main impact of the data-driven estimate is a reduction of the uncertainty by approximately a factor of two. The total systematic uncertainty on the fitted background prediction is computed taking into account all correlations and anti-correlations between the individual sources of systematic uncertainty. Agreement is found between the predicted and observed values in all regions within uncertainties.

Common criteria: lepton veto, $p_T^{j_1} > 90$ GeV, $\geqslant 3$ b-jets, $E_T^{miss}/m_{eff}^{4j} > 0.2$, $\Delta\phi_{min}^{4j} > 0.4$				
VR	N_J ($p_T > 50$ GeV)	p_T b-jets	E_T^{miss} [GeV]	m_{eff} [GeV]
VR4-1	≥ 4 jets	> 50 GeV	$150 < E_T^{miss} < 200$	$m_{eff}^{4j} > 500$
VR4-2	≥ 4 jets	> 50 GeV	$E_T^{miss} > 200$	$500 < m_{eff}^{4j} < 900$
VR6-1	≥ 6 jets	> 30 GeV	$150 < E_T^{miss} < 200$	$m_{eff}^{incl} > 600$
VR6-2	≥ 6 jets	> 30 GeV	$E_T^{miss} > 200$	$600 < m_{eff}^{incl} < 1100$

Table 3: Definition of the four validation regions.

9 Results and interpretation

Figure 2 shows the measured missing transverse momentum and effective mass distributions together with the MC predictions, normalised to cross-section times integrated luminosity, for the SM backgrounds in the SR4-L and SR6-L signal regions (see Table 1). Also shown are the predictions of two benchmark signal models. The results of the background fit to the control regions extrapolated to the signal regions, together with the nominal MC predictions for the $t\bar{t}$+jets and the total backgrounds, are shown in Tables 6 and 7. The numbers of events seen in the signal regions are consistent with the SM expectations.

Limits for non-SM signal at 95% confidence level (CL) are derived by testing the signal plus background hypothesis in each signal region with the CL_s prescription [45]. These limits are obtained with fits similar to those used to estimate the background in each signal region, except that the number of observed events in the signal region is added as an input to the fit and a second free parameter for the non-SM signal strength, constrained to be non-negative, is adjusted in the likelihood maximisation. Model-independent upper limits at 95% CL on the number of signal events and on the visible cross-section (defined as the production cross-section times kinematic acceptance times experimental efficiency) for non-SM contributions

channel	CR4	VR4-1	VR4-2
Observed events	2518	249	158
Total background events	2518 ± 80	291 ± 50	176 ± 30
(MC prediction)	(2400 ± 700)	(280 ± 100)	(170 ± 60)
$t\bar{t}$ + jets events	1936 ± 200	217 ± 40	126 ± 24
(MC prediction)	(1800 ± 600)	(210 ± 70)	(120 ± 40)
$t\bar{t} + b/b\bar{b}$ events	155 ± 150	46 ± 46	25 ± 25
single top events	125 ± 45	12 ± 5	8 ± 3
$t\bar{t} + W/Z$ events	28 ± 15	3 ± 2	4 ± 2
W/Z events	269 ± 120	12 ± 7	13 ± 8
diboson events	5 ± 3	–	–
Gbb : $m_{\tilde{g}} = 1000$ GeV, $m_{\tilde{\chi}_1^0} = 600$ GeV	39 ± 16	12 ± 2	29 ± 5
Gbb : $m_{\tilde{g}} = 1200$ GeV, $m_{\tilde{\chi}_1^0} = 1$ GeV	8.9 ± 5.5	0.1 ± 0.1	0.1 ± 0.1

Table 4: Results of the background fit to the control region CR4 extrapolated to the validation regions VR4-1 and VR4-2. Nominal MC expectations (normalised to MC cross-sections) for the $t\bar{t}$+jets and the total backgrounds are given for comparison. The yield for two signal points (with small and large mass splitting between the gluino and the LSP) for the *Gbb* ($\tilde{g} \to b\bar{b}\tilde{\chi}_1^0$) model are also shown. Statistical plus systematic uncertainties are shown. The systematic uncertainties include all detector related and theoretical uncertainties for the background, and only the detector related uncertainties for the signal.

channel	CR6	VR6-1	VR6-2
Observed events	255	52	34
Total background events	255 ± 20	55 ± 15	32 ± 9
(MC prediction)	(255 ± 100)	(55 ± 26)	(32 ± 17)
$t\bar{t}$ + jets events	205 ± 30	35 ± 8	20 ± 5
(MC prediction)	(205 ± 80)	(35 ± 16)	(20 ± 11)
$t\bar{t} + b/b\bar{b}$ events	24 ± 24	16 ± 16	9 ± 9
single top events	10 ± 4	2 ± 1	1 ± 1
$t\bar{t} + W/Z$ events	5 ± 3	1 ± 1	1 ± 1
W/Z events	11 ± 6	1 ± 1	2 ± 1
diboson events	–	–	–
Gtt : $m_{\tilde{g}} = 1000$ GeV, $m_{\tilde{\chi}_1^0} = 400$ GeV	15 ± 5	5.9 ± 0.6	8.6 ± 0.8
Gtt : $m_{\tilde{g}} = 1200$ GeV, $m_{\tilde{\chi}_1^0} = 1$ GeV	3.6 ± 1.6	0.2 ± 0.1	0.1 ± 0.1

Table 5: Results of the background fit to the control region CR6 extrapolated to the validation regions VR6-1 and VR6-2. Nominal MC expectations (normalised to MC cross-sections) for the $t\bar{t}$+jets and the total backgrounds are given for comparison. The yield for two signal points (with small and large mass splitting between the gluino and the LSP) for the Gtt ($\tilde{g} \to t\bar{t}\tilde{\chi}_1^0$) model are also shown. Statistical plus systematic uncertainties are shown. The systematic uncertainties include all detector related and theoretical uncertainties for the background, and only the detector related uncertainties for the signal.

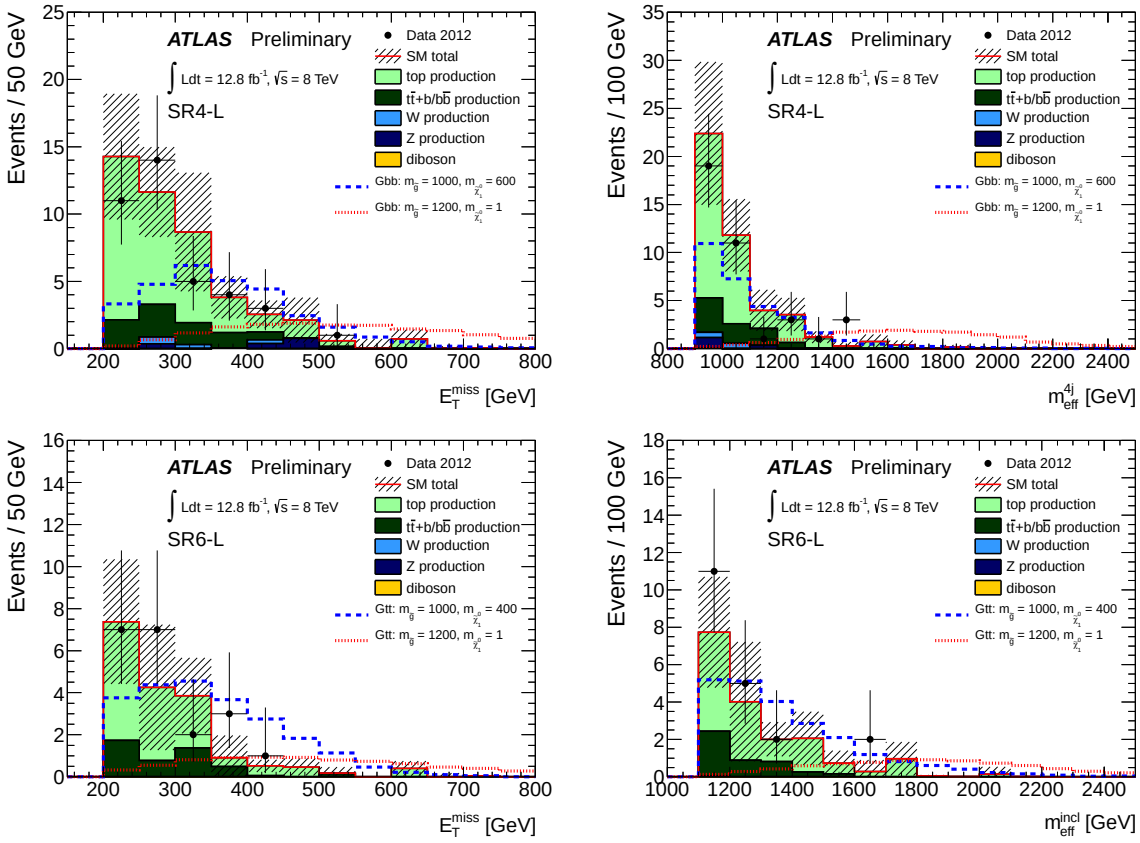

Figure 2: Distribution of the missing transverse momentum (left) and effective mass (right) in the SR4-L (top) and SR6-L (bottom) signal regions. The effective mass definition corresponds to m_{eff}^{4j} and $m_{\text{eff}}^{\text{incl}}$ in SR4-L and SR6-L, respectively. The MC expectation is normalised to cross-section times integrated luminosity. The hatched band shows the statistical uncertainty on the simulated event samples combined with the detector related systematic uncertainty (among which jet energy scale and b-tagging uncertainties are dominant). The histogram labelled "top production" includes the contribution from $t\bar{t}$ +jets, $t\bar{t}+W/Z$ and single top production. Two signal points (with small and large mass splitting between the gluino and the LSP) for the *Gbb* ($\tilde{g} \to bb\tilde{\chi}_1^0$) and *Gtt* ($\tilde{g} \to t\bar{t}\tilde{\chi}_1^0$) models are overlaid.

channel	SR4-L	SR4-M	SR4-T
Observed events	38	8	4
Total background events	46 ± 10	10.7 ± 2.9	2.9 ± 1.0
(MC prediction)	(44 ± 17)	(10.3 ± 4.6)	(2.7 ± 1.3)
$t\bar{t}$ + jets events	30 ± 6	7.0 ± 1.8	2.4 ± 0.9
(MC prediction)	(29 ± 11)	(6.6 ± 2.5)	(2.3 ± 1.1)
$t\bar{t} + b/b\bar{b}$ events	8.1 ± 8.3	2.5 ± 2.5	0.1 ± 0.2
single top events	3.5 ± 1.3	0.4 ± 0.5	0.2 ± 0.1
$t\bar{t} + W/Z$ events	1.4 ± 0.8	0.5 ± 0.3	0.2 ± 0.1
W/Z events	2.6 ± 1.9	0.4 ± 0.6	–
diboson events	–	–	–
Gbb : $m_{\tilde{g}} = 1000$ GeV, $m_{\tilde{\chi}_1^0} = 600$ GeV	30 ± 7	11 ± 3	3.8 ± 1.3
Gbb : $m_{\tilde{g}} = 1200$ GeV, $m_{\tilde{\chi}_1^0} = 1$ GeV	17 ± 2	17 ± 2	15 ± 2

Table 6: Results of the background fit to the control region CR4 extrapolated to the signal regions SR4-L, SR4-M and SR4-T. Nominal MC expectations (normalised to MC cross-sections) for the $t\bar{t}$+jets and the total backgrounds are given for comparison. The yield for two signal points (with small and large mass splitting between the gluino and the LSP) for the *Gbb* ($\tilde{g} \to b\bar{b}\tilde{\chi}_1^0$) model are also shown. Statistical plus systematic uncertainties are shown. The systematic uncertainties include all detector related and theoretical uncertainties for the background, and only the detector related uncertainties for the signal.

channel	SR6-L	SR6-M	SR6-T
Observed events	20	4	2
Total background events	18 ± 6	6.3 ± 2.4	2.2 ± 1.3
(MC prediction)	(18 ± 9)	(6.3 ± 3.4)	(2.2 ± 1.8)
$t\bar{t}$ + jets events	12 ± 4	4.3 ± 1.9	1.7 ± 1.0
(MC prediction)	(12 ± 6)	(4.3 ± 2.4)	(1.7 ± 1.5)
$t\bar{t} + b/b\bar{b}$ events	4.6 ± 5.0	1.3 ± 1.4	0.2 ± 0.3
single top events	0.6 ± 0.3	0.4 ± 0.2	0.2 ± 0.1
$t\bar{t} + W/Z$ events	0.8 ± 0.4	0.3 ± 0.2	0.1 ± 0.1
W/Z events	0.1 ± 0.1	–	–
diboson events	–	–	–
Gtt : $m_{\tilde{g}} = 1000$ GeV, $m_{\tilde{\chi}_1^0} = 400$ GeV	18 ± 3	8.8 ± 2.2	3.6 ± 1.2
Gtt : $m_{\tilde{g}} = 1200$ GeV, $m_{\tilde{\chi}_1^0} = 1$ GeV	8.2 ± 0.4	7.8 ± 0.5	6.8 ± 0.6

Table 7: Results of the background fit to the control region CR6 extrapolated to the signal regions SR6-L, SR6-M and SR6-T. Nominal MC expectations (normalised to MC cross-sections) for the $t\bar{t}$+jets and the total backgrounds are given for comparison. The yield for two signal points (with small and large mass splitting between the gluino and the LSP) for the Gtt ($\tilde{g} \rightarrow t\bar{t}\tilde{\chi}_1^0$) model are also shown. Statistical plus systematic uncertainties are shown. The systematic uncertainties include all detector related and theoretical uncertainties for the background, and only the detector related uncertainties for the signal.

derived for each signal region are given in Table 8. These upper limits are derived assuming no signal contribution in the control regions and no detector related systematic uncertainties on the signal. When the results are interpreted in the framework of specific SUSY scenarios, the additional free parameter for the non-SM signal strength ensures a proper treatment of the expected signal contribution in the control regions.

SR	95% CL UL on N_{BSM}		95% CL UL on $\sigma \times \mathscr{A} \times \varepsilon$ [fb]	
	Observed	Expected	Observed	Expected
SR4-L	17.9	$20.5^{+8.0}_{-5.2}$	1.4	1.6
SR4-M	7.6	$8.8^{+3.5}_{-2.1}$	0.59	0.69
SR4-T	6.5	$5.0^{+2.2}_{-1.1}$	0.51	0.39
SR6-L	17.0	$15.5^{+6.2}_{-3.8}$	1.3	1.2
SR6-M	5.9	$6.6^{+2.8}_{-1.5}$	0.46	0.52
SR6-T	5.1	$4.6^{+1.9}_{-0.6}$	0.40	0.36

Table 8: Observed and expected new physics-model independent upper limits at 95% CL for the six signal regions. Limits are given on the number of signal events N_{BSM} and in terms of visible cross-section, defined as the cross-section times kinematic acceptance times experimental efficiency. The systematic uncertainties on the SM background estimation discussed in Section 7 are included.

These data have been used to derive limits in the parameter space of the following SUSY models:

***Gbb* model:** Simplified scenarios, where $\tilde{b}_1$ is the lightest squark but $m_{\tilde{g}} < m_{\tilde{b}_1}$. Pair production of gluinos is the only process taken into account since the masses of all other sparticles apart from the $\tilde{\chi}_1^0$ are set above the TeV scale. A three-body decay via an off-shell sbottom is assumed for the gluino, yielding a 100% BR for the decay $\tilde{g} \to b\bar{b}\tilde{\chi}_1^0$. The sbottom mass has no impact on the kinematics of the decay and the exclusion limits are presented in the $(m_{\tilde{g}}, m_{\tilde{\chi}_1^0})$ plane.

***Gtt* model:** Simplified scenarios, where $\tilde{t}_1$ is the lightest squark but $m_{\tilde{g}} < m_{\tilde{t}_1}$. Pair production of gluinos is the only process taken into account since the mass of all other sparticles apart from the $\tilde{\chi}_1^0$ are above the TeV scale. A three-body decay via off-shell stop is assumed for the gluino, yielding a 100% BR for the decay $\tilde{g} \to t\bar{t}\tilde{\chi}_1^0$. The stop mass has no impact on the kinematics of the decay and the exclusion limits are presented in the $(m_{\tilde{g}}, m_{\tilde{\chi}_1^0})$ plane.

The SR4 regions are mostly sensitive to the gluino decay $\tilde{g} \to b\bar{b}\tilde{\chi}_1^0$, whilst the SR6 regions are used to set exclusion limits in models with $\tilde{g} \to t\bar{t}\tilde{\chi}_1^0$. The signal region with the best expected sensitivity at each point in the parameter space is used to derive the limits at 95% CL. The experimental systematic uncertainties on the signal are treated as fully correlated with those obtained for the background. They are dominated by the JES and b-tagging uncertainties, which typically amount to 2-25% depending on the signal region and model considered. Signal cross-sections are calculated to next-to-leading order in the strong coupling constant, adding the resummation of soft gluon emission at next-to-leading-logarithmic accuracy (NLO+NLL) [46–50]. The nominal cross-section and the uncertainty are taken from an envelope of cross-section predictions using different PDF sets and factorisation and renormalisation scales, as described in Ref. [51]. The expected and observed 95% CL exclusion limits in

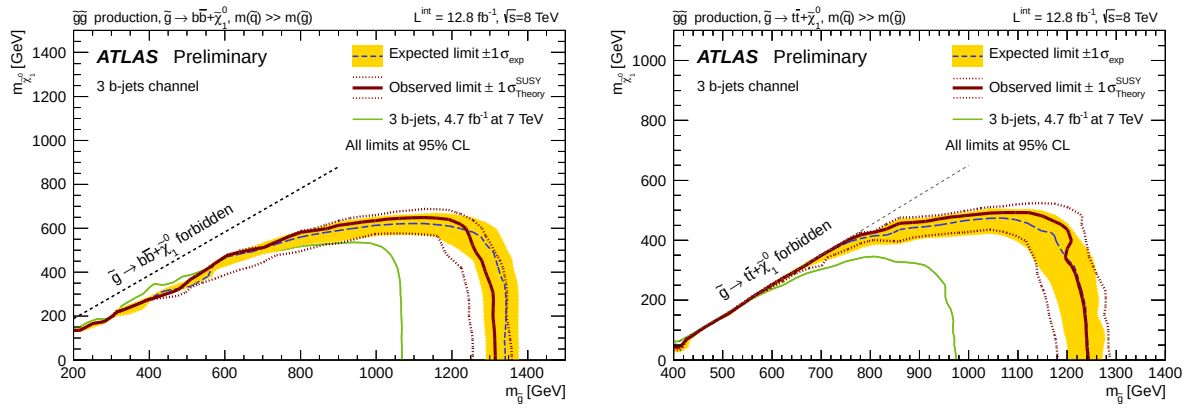

Figure 3: Exclusion limits in the $(m_{\tilde{g}}, m_{\tilde{\chi}_1^0})$ plane for the *Gbb* (left) and *Gtt* (right) models. The dashed blue and solid bold red lines show the 95% CL expected and observed limits respectively, including all uncertainties except the theoretical signal cross-section uncertainty. The shaded (yellow) bands around the expected limits show the impact of the experimental uncertainties while the dotted red lines show the impact on the observed limit of the variation of the nominal signal cross-section by 1σ theoretical uncertainty. Also shown for reference are the results of the previous analysis [19].

the two models considered above are shown in Figure 3.

In the context of the *Gbb* model, gluino masses below 1240 GeV are excluded for $m_{\tilde{\chi}_1^0} <$ 200 GeV while neutralino masses below 570 GeV are excluded for $m_{\tilde{g}} = 1100$ GeV, using the conservative $-1\sigma^{\text{SUSY}}_{\text{Theory}}$ hypothesis. It should be noted that the theoretical uncertainties at high gluino mass are large and are dominated by those originating from the PDF. For example, the theoretical uncertainty on the cross-section of pair production of 1.1 TeV and 1.3 TeV gluinos are 29% and 35% respectively. The signal region SR4-T has the best sensitivity at high gluino masses where the signal acceptance times efficiency reaches 30%, while the looser SR4-L and SR-M have a better sensitivity at low gluino masses and low mass splitting between the gluino and the neutralino due to their softer $m_{\text{eff}}^{\text{4j}}$ cuts. No sensitivity is achieved at very low mass splitting due to the very soft jets and the low $E_{\text{T}}^{\text{miss}}$ expected in signal events. This search extends the exclusion limits on the gluino mass from the previous analysis carried out with 4.7 fb^{-1} at 7 TeV [19] by approximatively 250 GeV.

In the context of the *Gtt* model, gluino masses below 1150 GeV are excluded for $m_{\tilde{\chi}_1^0} <$ 200 GeV while neutralino masses below 440 GeV are excluded for $m_{\tilde{g}} = 1100$ GeV. The signal region SR6-T has the best sensitivity at large mass splitting between the gluino and the neutralino, where hard jets and $E_{\text{T}}^{\text{miss}}$ are expected leading to a signal acceptance times efficiency of approximatively 13%, while the looser signal regions have a better sensitivity close to the diagonal because of the softer $m_{\text{eff}}^{\text{incl}}$ cut. This search extends the exclusion limits on the gluino mass from the previous analysis carried out with 4.7 fb^{-1} at 7 TeV [19] by approximatively 250 GeV.

10 Conclusions

In summary, this note presents results for gluino pair production with multi-*b*-jets final states in pp collisions at $\sqrt{s} = 8$ TeV, based on 12.8 fb^{-1} of ATLAS data. The events are selected with large $E_{\text{T}}^{\text{miss}}$, greater than or equal to four or six jets and at least three jets originating from *b*-quarks in the final state. The results are in agreement with the SM background prediction and

translate into 95% CL upper limits on excluded masses for two SUSY scenarios. Gluino masses up to 1.24 TeV are excluded, depending on the model, which significantly extends the previous results obtained with 4.7 fb^{-1} of data collected in 2011 at a centre-of-mass energy of 7 TeV.

References

[1] H. Miyazawa, *Baryon Number Changing Currents*, Prog. Theor. Phys. **36 (6)** (1966) 1266–1276.

[2] P. Ramond, *Dual Theory for Free Fermions*, Phys. Rev. D **3** (1971) 2415–2418.

[3] Y. Golfand and E. Likhtman, *Extension of the Algebra of Poincare Group Generators and Violation of p Invariance*, JETP Lett. **13** (1971) 323–326.

[4] A. Neveu and J. H. Schwarz, *Factorizable dual model of pions*, Nucl. Phys. B **31** (1971) 86–112.

[5] A. Neveu and J. H. Schwarz, *Quark Model of Dual Pions*, Phys. Rev. D **4** (1971) 1109–1111.

[6] J. Gervais and B. Sakita, *Field theory interpretation of supergauges in dual models*, Nucl. Phys. B **34** (1971) 632–639.

[7] D. Volkov and V. Akulov, *Is the Neutrino a Goldstone Particle?*, Phys. Lett. B **46** (1973) 109–110.

[8] J. Wess and B. Zumino, *A Lagrangian Model Invariant Under Supergauge Transformations*, Phys. Lett. B **49** (1974) 52.

[9] J. Wess and B. Zumino, *Supergauge Transformations in Four-Dimensions*, Nucl. Phys. B **70** (1974) 39–50.

[10] S. Weinberg, *Implications of Dynamical Symmetry Breaking*, Phys. Rev. D **13** (1976) 974–996.

[11] E. Gildener, *Gauge Symmetry Hierarchies*, Phys. Rev. D **14** (1976) 1667.

[12] S. Weinberg, *Implications of Dynamical Symmetry Breaking: An Addendum*, Phys. Rev. D **19** (1979) 1277–1280.

[13] L. Susskind, *Dynamics of Spontaneous Symmetry Breaking in the Weinberg- Salam Theory*, Phys. Rev. D **20** (1979) 2619–2625.

[14] P. Fayet, *Supersymmetry and Weak, Electromagnetic and Strong Interactions*, Phys. Lett. B **64** (1976) 159.

[15] P. Fayet, *Spontaneously Broken Supersymmetric Theories of Weak, Electromagnetic and Strong Interactions*, Phys. Lett. B **69** (1977) 489.

[16] G. R. Farrar and P. Fayet, *Phenomenology of the Production, Decay, and Detection of New Hadronic States Associated with Supersymmetry*, Phys. Lett. B **76** (1978) 575–579.

[17] P. Fayet, *Relations Between the Masses of the Superpartners of Leptons and Quarks, the Goldstino Couplings and the Neutral Currents*, Phys. Lett. B **84** (1979) 416.

[18] S. Dimopoulos and H. Georgi, *Softly Broken Supersymmetry and SU(5)*, Nucl. Phys. B **193** (1981) 150.

[19] ATLAS Collaboration, *Search for top and bottom squarks from gluino pair production in final states with missing transverse energy and at least three b-jets with the ATLAS detector*, arXiv:1207.4686 [hep-ex]. Accepted by Eur. Phys. J. C.

[20] ATLAS Collaboration, *The ATLAS Experiment at the CERN Large Hadron Collider*, J. Instrum. **3** (2008) S08003.

[21] S. Frixione, P. Nason, and C. Oleari, *Matching NLO QCD computations with Parton Shower simulations: the POWHEG method*, J. High Energy Phys. **0711** (2007) 070, arXiv:0709.2092 [hep-ph].

[22] T. Sjöstrand, S. Mrenna, and P. Z. Skands, *PYTHIA 6.4 Physics and Manual*, J. High Energy Phys. **0605** (2006) 026, arXiv:hep-ph/0603175 [hep-ph].

[23] H.-L. Lai et al., *New parton distributions for collider physics*, Phys. Rev. D **82** (2010) 074024, arXiv:1007.2241 [hep-ph].

[24] B. P. Kersevan and E. Richter-Was, *The Monte Carlo event generator AcerMC version 2.0 with interfaces to PYTHIA 6.2 and HERWIG 6.5*, arXiv:hep-ph/0405247 [hep-ph].

[25] J. Pumplin et al., *New generation of parton distributions with uncertainties from global QCD analysis*, J. High Energy Phys. **0207** (2002) 012, arXiv:hep-ph/0201195 [hep-ph].

[26] S. Frixione and B. R. Webber, *The MC@NLO 3.2 event generator*, arXiv:hep-ph/0601192 [hep-ph].

[27] G. Corcella et al., *HERWIG 6: An Event generator for hadron emission reactions with interfering gluons (including supersymmetric processes)*, J. High Energy Phys. **0101** (2001) 010, arXiv:hep-ph/0011363 [hep-ph].

[28] J. Butterworth et al., *Multiparton interactions in photoproduction at HERA*, Z. Phys. C **72** (1996) 637–646.

[29] T. Gleisberg et al., *Event generation with SHERPA 1.1*, J. High Energy Phys. **0902** (2009) 007, arXiv:0811.4622 [hep-ph].

[30] M. Bähr et al., *Herwig++ Physics and Manual*, Eur. Phys. J. C **58** (2008) 639–707.

[31] ATLAS Collaboration, *The ATLAS Simulation Infrastructure*, Eur. Phys. J. C **70** (2010) 823–874, arXiv:1005.4568 [physics.ins-det].

[32] S. Agostinelli et al., *Geant4a simulation toolkit*, Nucl. Instrum. Meth. A **506** (2003) 250–303. http://www.sciencedirect.com/science/article/pii/S0168900203013688.

[33] M. Cacciari, G. Salam, and G. Soyez, *The anti-k_t jet clustering algorithm*, J. High Energy Phys. **0804** (2008) 063, arXiv:0802.1189 [hep-ph].

[34] M. Cacciari and G. Salam, *Dispelling the N3 myth for the kt jet-finder*, Phys. Lett. B **641** no. 1, (2006) 57 – 61.

[35] ATLAS Collaboration, *Jet energy measurement with the ATLAS detector in proton-proton collisions at sqrt(s) = 7 TeV*, arXiv:1112.6426 [hep-ex]. submitted to Eur. Phys. J. C.

[36] ATLAS Collaboration, *Measurement of the b-tag Efficiency in a Sample of Jets Containing Muons with 5 fb^{-1} of Data from the ATLAS Detector*, ATLAS-CONF-2012-043 (2012). http://cdsweb.cern.ch/record/1435197.

[37] ATLAS Collaboration, *b-jet tagging calibration on c-jets containing D* mesons*, ATLAS-CONF-2012-039 (2012). http://cdsweb.cern.ch/record/1435193.

[38] ATLAS Collaboration, *Measurement of the Mistag Rate of b-tagging algorithms with 5 fb^{-1} of Data Collected by the ATLAS Detector*, ATLAS-CONF-2012-040 (2012). http://cdsweb.cern.ch/record/1435194.

[39] ATLAS Collaboration, *Electron performance measurements with the ATLAS detector using the 2010 LHC proton-proton collision data*, Eur. Phys. J. C **72** (2012) 1909, arXiv:1110.3174 [hep-ex].

[40] ATLAS Collaboration, *Search for squarks and gluinos with the ATLAS detector in final states with jets and missing transverse momentum using 4.7 fb-1 of sqrt(s) = 7 TeV proton-proton collision data*, arXiv:1208.0949 [hep-ex]. submitted to Phys. Rev. D.

[41] ATLAS Collaboration, *Single hadron response measurement and calorimeter jet energy scale uncertainty with the ATLAS detector at the LHC*, arXiv:1203.1302 [hep-ex]. submitted to Eur. Phys. J. C.

[42] M. L. Mangano, M. Moretti, F. Piccinini, R. Pittau, and A. D. Polosa, *ALPGEN, a generator for hard multiparton processes in hadronic collisions*, J. High Energy Phys. **07** (2003) 001, arXiv:hep-ph/0206293.

[43] ATLAS Collaboration, *Measurement of $t\bar{t}$ production with a veto on additional central jet activity in pp collisions at sqrt(s) = 7 TeV using the ATLAS detector*, Eur. Phys. J. C **72** (2012) 2043, arXiv:1203.5015 [hep-ex].

[44] ATLAS Collaboration, *Luminosity determination in pp collisions at sqrt(s) = 7 TeV using the ATLAS detector in 2011*, ATLAS-CONF-2011-116 (2011). http://cdsweb.cern.ch/record/1376384.

[45] G. Cowan et al., *Asymptotic formulae for likelihood-based tests of new physics*, Eur. Phys. J. C **71** (2011) 1554.

[46] W. Beenakker et al., *Squark and gluino production at hadron colliders*, Nucl. Phys. B **492** (1997) 51–103, arXiv:hep-ph/9610490 [hep-ph].

[47] A. Kulesza and L. Motyka, *Threshold resummation for squark-antisquark and gluino-pair production at the LHC*, Phys. Rev. Lett. **102** (2009) 111802, arXiv:0807.2405 [hep-ph].

[48] A. Kulesza and L. Motyka, *Soft gluon resummation for the production of gluino-gluino and squark-antisquark pairs at the LHC*, Phys. Rev. D **80** (2009) 095004, arXiv:0905.4749 [hep-ph].

[49] W. Beenakker et al., *Soft-gluon resummation for squark and gluino hadroproduction*, J. High Energy Phys. **0912** (2009) 041, arXiv:0909.4418 [hep-ph].

[50] W. Beenakker et al., *Squark and gluino hadroproduction*, Int. J. Mod. Phys. A **26** (2011) 2637–2664, arXiv:1105.1110 [hep-ph].

[51] M. Krämer et al., *Supersymmetry production cross sections in pp collisions at sqrts = 7 TeV*, arXiv:1206.2892 [hep-ph].